Check for updates

Regulating the thermal conductivity of monolayer MnPS₃ by a magnetic phase transition†

Dingbo Zhang,‡[a,b] Ke Wang,‡[c] Shuai Chen, [ID] [b] Lifa Zhang,[d] Yuxiang Ni [ID] *[a] and Gang Zhang [ID] *[b]

In this study, based on *ab initio* calculations and the phonon Boltzmann transport equation, we found that magnetic phase transitions can lead to a significant change in the thermal conductivity of monolayer MnPS₃. Around the Néel temperature (78 K) with the antiferromagnetic–paramagnetic (AFM–PM) phase transition, its thermal conductivity increases from 14.89 W mK^{-1} (AFM phase) to 103.21 W mK^{-1} (PM phase). Below 78 K, the thermal conductivity of monolayer MnPS₃ can be doubled by applying a magnetic field of 4 T, this value has been reported in a previous experiment for the antiferromagnetic–ferromagnetic (AFM–FM) phase transition. Above 78 K, the thermal conductivity of PM phase can be greatly reduced through the PM–AFM magnetic phase transition. In addition to the value of thermal conductivity, the relative contribution ratio between acoustic and optical modes changes with different magnetic phases. The subsequent analyses demonstrate that this regulation originates from the change in lattice parameter, bonding interaction and phonon anharmonicity. In addition, the different effect on the thermal conductivity between the FM and AFM phases was identified by comparing the corresponding phonon scattering characteristics. This study should shed light on the understanding of phonon thermal conductivity in 2D magnets, and provide a practical method for the realization of 2D thermal switching devices, which would enable a broad range of novel applications including energy conversion and thermal management.

1 Introduction

Two-dimensional (2D) magnetic materials retain long-range magnetic ordering in the individual monolayer.[1–3] By manipulating the spin degree of freedom of the electron, the data processing speed and integration densities of 2D magnetic materials can be largely enhanced.[4,5] Thus, 2D magnetic materials act as a good playground to explore future information technologies. One significant challenge that magnetic-based devices are facing is the heat dissipation issue, which directly affects the working state and operational stability.[6,7] In this regard, it is imperative to obtain fundamental understanding of the thermal conductivity of 2D magnetic materials.[8–10]

In recent years, progress has been made in understanding the magnetic ordering impact on the thermal transport of 2D magnetic materials. For instance, semi-hydrogenated graphene bears a higher thermal conductivity in its FM phase (55.7 W mK^{-1}) than in the paramagnetic (PM) phase (24.5 W mK^{-1}).[6] For monolayer CrI₃, the magnetic state enhances the thermal conductivity because it induces a more symmetric structure with weaker phonon anharmonicity.[7] It should be mentioned that antiferromagnets have drawn more attention than ferromagnets,[11–13] owing to their several advantages including spin superfluidity,[14] ultrafast dynamics[15] and the negligible spin–dipole interaction.[16] Unfortunately, little is known about the thermal conductivity in 2D antiferromagnetic materials.

Recently, 2D MnPS₃, one novel antiferromagnet, was obtained through chemical exfoliation.[17] The unit cell of monolayer MnPS₃ is composed of two Mn^{2+} ions and one [P₂S₆]$^{4-}$, forming a hexagonal honeycomb lattice, as shown in Fig. 1.[18] So, the antiferromagnetic configuration in the MnPS₃ unit cell is described as one Mn atom which is spin-up and the other one is spin-down. In addition, 2D MnPS₃ is one direct bandgap semiconductor, sharing ultrafast domain-wall dynamics and the spin photogalvanic effect.[15,19] Excitons in

[a]School of Physical Science and Technology, Southwest Jiaotong University, Chengdu 610031, China. E-mail: yuxiang.ni@swjtu.edu.cn
[b]Institute of High Performance Computing, A*STAR, 138632, Singapore. E-mail: zhangg@ihpc.a-star.edu.sg
[c]School of Automation, Xi'an University of Posts & Telecommunications, Shaanxi, 710121, China
[d]NNU-SULI Thermal Energy Research Center, and Center for Quantum Transport and Thermal Energy Science (CQTES), School of Physics and Technology, Nanjing Normal University, Nanjing 210023, China

†Electronic supplementary information (ESI) available. See DOI: https://doi.org/10.1039/d2nr04709h
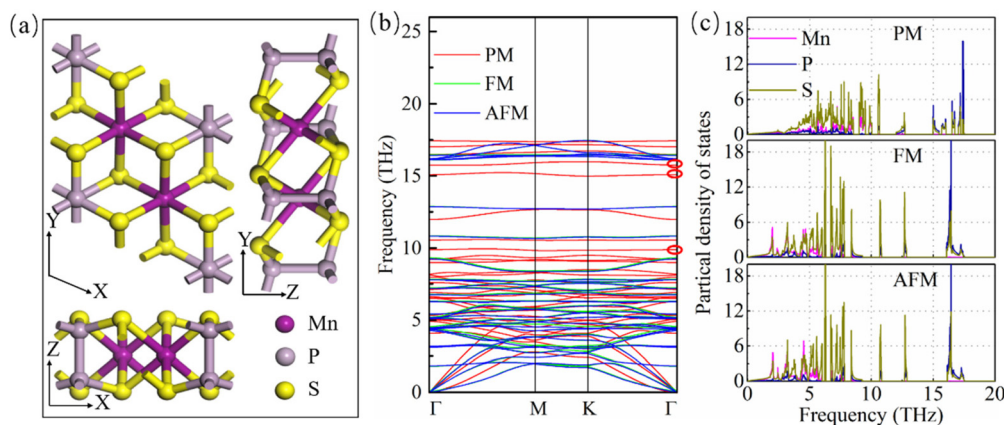‡Authors contributed equally to this work.

Fig. 1 The structure and phonon behaviors. (a) Atomic structure of monolayer MnPS$_3$. (b) Phonon dispersions and (c) phonon density of states of monolayer MnPS$_3$ with PM/FM/AFM phases.

MnPS$_3$ are bound by an energy of more than 1 eV, exceeding the values in transition-metal dichalcogenides, advancing this 2D antiferromagnet as a new platform for exploring the magnetic and phononic properties.[20]

In this work, we investigated the structures, lattice vibrations and thermal conductivities of monolayer MnPS$_3$ with PM, ferromagnetic (FM) and antiferromagnetic (AFM) phases. We found that, through the PM–AFM phase change, the phonon anharmonicity of monolayer MnPS$_3$ obviously increased and the thermal conductivity decreased by one order of magnitude. Meanwhile, the AFM phase has lower thermal conductivity compared with its FM counterpart. The phonon mean free path (MFP), group velocity and phonon scattering strength were analyzed to reveal the underling physical mechanism.

2   Computational methods

The first-principles calculations were performed using Density Functional Theory (DFT) as implemented in the Vienna *Ab initio* Simulation Package (VASP).[21] The Perdew–Burke–Ernzerhof (PBE) exchange–correlation functional was used.[22] A Hubbard *U* correction was included.[23] When the exchange parameter for Mn 3d-electrons was fixed as *U* = 5 eV, the calculated electronic band-gap (2.70 eV) of MnPS$_3$ is close to the experimental value of 2.96 eV.[17] Therefore, the same value of *U* was used to compute all the properties of the PM, FM and AFM phases. As DFT is a ground state theory, in principle, it cannot deal with the PM phase. In our DFT calculations, the PM phase is in fact a nonmagnetic phase, *i.e.*, the spin-polarization is switched off and no spin or magnetism exists in the calculations. In the structural optimization, the convergence criteria for the electronic and ionic relaxations are 10^{-8} eV and 10^{-4} eV Å^{-1}, respectively. The *K*-mesh of 25 × 25 × 1 and cut-off energy of 500 eV are used. A vacuum length of 20 Å is adopted to eliminate the interaction between neighboring layers. Before calculating the phononic properties, the magnetic

ground state of monolayer MnPS$_3$ was determined by the energy difference between possible magnetic configurations (FM, AFM-zigzag, AFM-stripy, and AFM-Néel) as shown in Fig. S1 in the ESI,† and we find that the AFM-Néel state is the magnetic ground state because of its lowest energy. In the following, the AFM state means AFM-Néel state. Calculations of the second- and third-order force constants were carried out by using Phonopy and thirdorder.py, respectively.[24,25] Additionally, it was found that the higher-order force constants have little impact on the thermal conductivity of 2D materials at low temperatures (<200 K), as shown in Table S2.† [26,27] Therefore, in our work, only second- and third-order force constants are considered. The thermal conductivity was calculated by solving the phonon Boltzmann transport equation as implemented in ShengBTE.[28] After structure optimization, 10.67, 7.69 and 7.76 Å are used as the thickness of the monolayer MnPS$_3$ with PM, FM and AFM phases, respectively. The thickness of the monolayer is equal to the height of a bulk cell in the *Z* direction divided by the corresponding number of atomic layers. Details of the calculation can be found in ESI.†

3   Results and discussion

3.1   Structure, phonon dispersion and phonon density of states

We firstly investigated the influence of magnetic ordering on the structural parameters. As shown in Fig. 1, the phonon dispersions are located in a frequency range of 0–18 THz and there appear no imaginary frequencies throughout the entire Brillouin zone, suggesting the dynamical stability of all these three phases. The optimized lattice constants and bond lengths of the FM and AFM phases are quite close but both are larger than those of the PM phase (Table 1). The calculated structural parameters of the AFM phase are consistent with previous reports.[29,30] To identify the accuracy of our calculation, we did a comprehensive review on the experimental

Table 1 Lattice constant, bond length and layer thickness in the PM/FM/AFM MnPS$_3$

Properties	PM	FM	AFM
Lattice constant (Å)	5.70	6.14	6.15
Mn–S bond length (Å)	2.45	2.61	2.63
P–S bond length (Å)	3.26	3.38	3.40
Layer thickness (Å)	10.67	7.69	7.76

and theoretical lattice constants of MnPS$_3$ at various magnetic states and the lattice constants are summarized in Table S1.†

Based on the frozen magnon method, the relationship of the harmonic IFCs between FM (AFM) and PM structures is described by the following formula:

$$\tilde{F}_{\vec{R}i\alpha\vec{R}'j\beta} = F_{\vec{R}i\alpha\vec{R}'j\beta} - \sum_{mn} J''_{\vec{R}i\alpha\vec{R}'j\beta;mn} \langle \vec{S}_m \cdot \vec{S}_n \rangle,$$

where $\tilde{F}$ and F are the harmonic IFCs in the FM(AFM) and PM phases, respectively. J'' stands for the second derivative of magnetic exchange interaction J. The movement of atom i is marked by $\vec{R}(\vec{R}')$ lattice vector along the $\alpha(\beta)$ Cartesian direction. S is equal to half of the spin number in a magnetic atom. The J'' of FM and AFM phases can be calculated via the interatomic force constants (Fig. 2). It is obvious that the IFCs of AFM and FM states are similar, while the difference in IFCs between PM and AFM states is quite significant, resulting in the difference in the lattice constant between PM and AFM states is up to 0.45 Å. This is similar to the previous theoretical results about the difference in lattice constant between the PM[31,32] and AFM states.[31] Similar phenomena were also observed in bulk MnPS$_3$.[31,33]

With 10 atoms in the unit cell, monolayer MnPS$_3$ has 3 acoustic and 27 optical phonon modes. To better observe the difference in phonon dispersions among PM, FM and AFM phases, we presented them in Fig. 1(b), while more details are presented in Fig. S2.† The phonon branches in the FM and AFM phases are similar, which are different from that in the PM phase. Next, we mainly focused on the three optical branches of the PM structure, which are located in the gap of the FM/AFM phases (marked by red circle). The corresponding vibration modes are presented in Fig. S3† and their irreducible representations are A$_{1g}$, A$_{2g}$ and A$_{2u}$ modes, respectively. These three lattice vibration modes are identified in the FM/AFM phases. The frequencies of these three optical branches are 9.90, 15.09 and 15.76 THz at Γ point in the PM phase, while these values are 5.18 (5.21), 16.11 (16.12) and 16.15 (16.15) THz in the FM (AFM) phase, respectively. The appearance of the large splitting between PM and FM/AFM phases for the three optical branches is mainly due to the sensitivity of the atoms in MnPS$_3$ to the magnetic ordering, which induces the down- and up-shift of optical phonon modes mainly contributed by Mn atoms and other atoms, respectively. The phonon projected density of states (pDOS) shown in Fig. 1(c) confirms the shift of optical phonons, which also demonstrates the red-shift of acoustic phonon modes in the AFM/FM phases compared with the PM phase. These results indicate significant coupling between spin and phonon in the FM and AFM monolayer MnPS$_3$.

3.2 The magnetic ordering-dependent thermal conductivity

In order to explore the impact of magnetic ordering on the thermal conductivity, the thermal conductivities of monolayer MnPS$_3$ with PM, FM and AFM phases were calculated, respectively. As shown in Fig. 3(a) on a log–log scale, the thermal conductivity of monolayer MnPS$_3$ decreases as temperature (T) increases, following a $1/T$ dependence, confirming that the phonon–phonon anharmonic scattering plays a major role in the thermal conductivity of monolayer MnPS$_3$. Near the Néel temperature (78 K) of MnPS$_3$, the thermal conductivity of the PM phase is 103.21 W mK^{-1}, seven times as large as that of the AFM phase (14.89 W mK^{-1}). For FM ordering, the thermal conductivity (27.35 W mK^{-1}) is only 26% of that of the PM phase. The magnetic ordering effectively changes the thermal conductivity of monolayer MnPS$_3$, which has never been reported in the literature. The ratio between the thermal conductivity of different phases ($\kappa_{PM} : \kappa_{AFM} = 6.93$ and $\kappa_{PM} : \kappa_{FM} = 3.77$) is comparable to those of reported theoretical works such as RuCl$_3$ ($\kappa_{FM} : \kappa_{PM} = 6.23$), RuBr$_3$ ($\kappa_{FM} : \kappa_{PM} = 6.87$) and RuI$_3$ ($\kappa_{FM} : \kappa_{PM} = 1.59$).[9] In experiments, below 78 K, the thermal conductivity of monolayer MnPS$_3$ can be doubled by applying an magnetic field perpendicular to the layer, where the critical value of the magnetic field for the AFM–FM phase transition is about 4 T.[17] Above 78 K, the thermal conductivity can be greatly reduced through external magnetic fields, this method has been demonstrated to induce a PM–AFM magnetic phase transition.[1,34] Thus, the large modulation of the
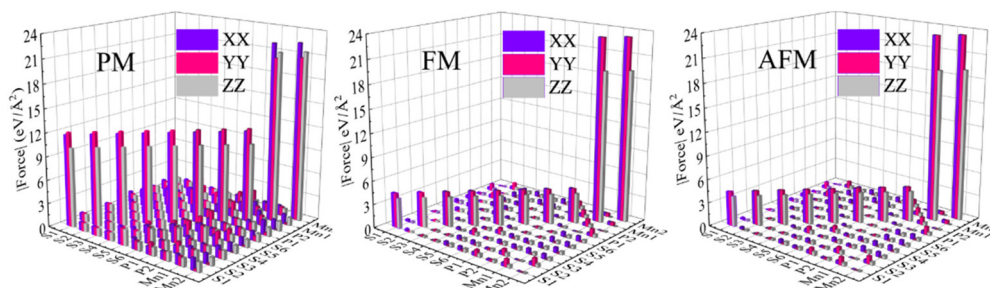
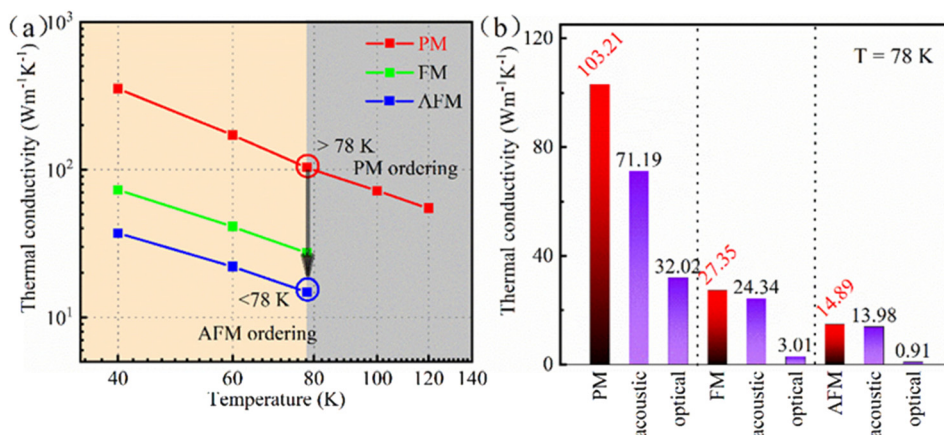**Fig. 2** Interatomic force constants of PM, FM and AFM MnPS$_3$.

Fig. 3 The thermal conductivity. (a) The magnetic ordering-dependent thermal conductivities and (b) contribution of acoustic and optical modes to the thermal conductivities at 78 K.

thermal conductivity of monolayer $MnPS_3$ provides a practical method for the realization of 2D thermal switching devices.

In these three magnetic phases, acoustic phonons are still the major contributors to the thermal conductivity but the relative contribution ratio between acoustic and optical modes changes with different magnetic phases (Fig. 3(b)). This behavior also occurs in hydrogenated graphene.[6] Recently, the impact of the four-phonon scattering process on the thermal conductivity of solids have attracted extensive research attention.[35,36] Compared with the relaxation time of phonons in the low frequency range, the relaxation time of phonons in the high frequency range (*i.e.*, optical modes) will be reduced more significantly by the four-phonon scattering processes.[37] For PM/AFM/FM $MnPS_3$, the thermal conductivity contributed by the optical phonons is low. Thus, the four-phonon scattering process is not considered in our work. To understand the underlying physical mechanism of the tunable thermal conductivity, we analyzed the phonon mean free path, group velocity and phonon scattering strength.

3.3 The magnetic ordering-dependent phonon properties

It is obvious from Fig. 4(a) that the normalized cumulative thermal conductivity increases as the phonon mean free path (MFP) increases until it reaches a limit length, which is 1835.58, 3125.71 and 16681.01 nm for the AFM, FM and PM phases, respectively. This suggests that the MFP of the PM phase is longer than that of FM and AFM phases, which results in a larger thermal conductivity. Fig. 4(b) presents the group velocities of three acoustic branches (ZA: out-of-plane acoustic, TA: transverse acoustic and LA: longitudinal acoustic) and optical branches varying with frequency. Specifically, the impact of magnetic ordering on phonon velocity is more remarkable for the three acoustic branches. The maximum phonon group velocities of acoustic phonon modes gradually decrease from PM to FM to AFM phases, as shown in Table S3.† Therefore, the reduced group velocity in the FM and AFM phases is also responsible for the lower thermal conductivity. However, compared with the large change in MFP, the change in group velocity is slight, revealing the remarkable
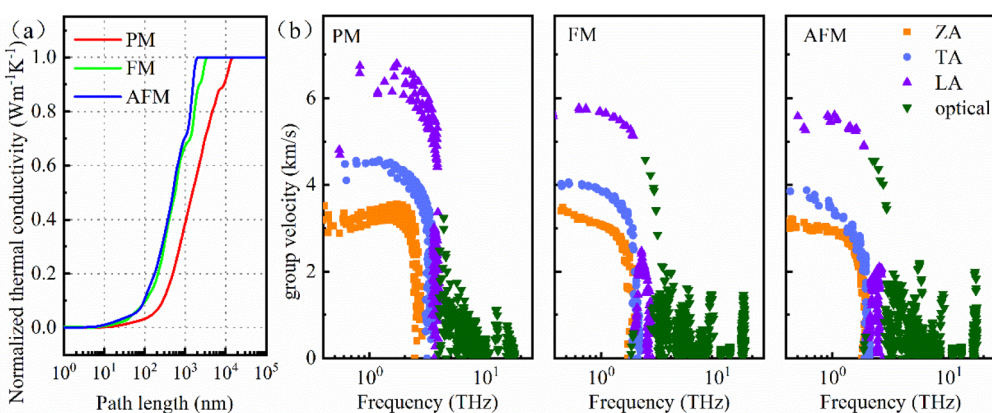

Fig. 4 The magnetic ordering-dependent phonon behaviors. (a) Mean free paths and (b) frequency-resolved phonon group velocities of the PM/FM/AFM phases.
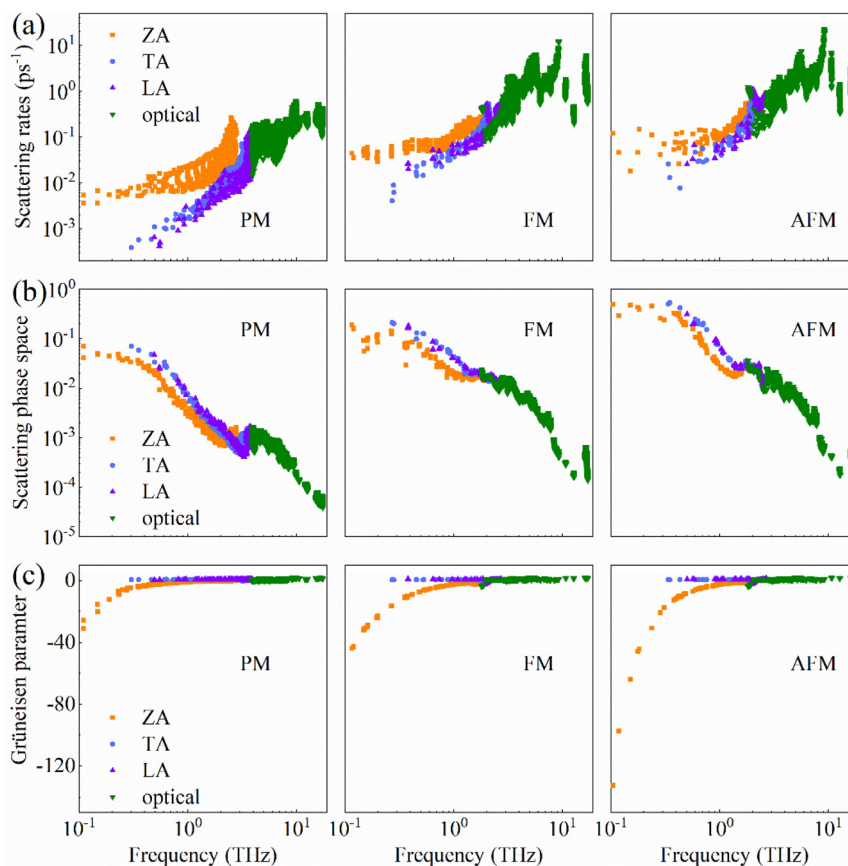
Fig. 5 The magnetic ordering-dependent phonon scattering characteristics. (a) Anharmonic scattering rates, (b) scattering phase spaces and (c) Grüneisen parameters for the PM/FM/AFM phases.

impact of magnetic ordering on phonon anharmonicity in monolayer MnPS$_3$.

Phonon scattering strength and phonon anharmonicity of these three magnetic phases were evaluated by calculating the scattering rate, the scattering phase space and the Grüneisen parameter.[38,39] These parameters reflect the scattered possibility in unit time, the number of channels available for a phonon to be scattered and the phonon anharmonicity, respectively.[40] As presented in Fig. 5(a) and Fig. S4,† the phonon–phonon anharmonic scattering rate and phonon-isotope scattering rate in AFM/FM phases are obviously higher than that in the PM phase, which implies that the phonon relaxation time is shortened. Fig. 5(b) shows that the AFM/FM phases have a greater value of scattering phase space than the PM phase at the same frequency, which implies that the former phases hold more scattering channels than the latter one. The scattering phase space gradually decreases with the increase of phonon frequency, which was also observed in 2D group-IV materials.[41] This is a consequence of the fact that the phonon branches at low frequencies are denser (Fig. 1(b)), which causes more phonon scattering possibility in accordance with the requirement of energy and momentum conservation.

As shown in Fig. 5(c), the Grüneisen parameters of the AFM/FM phases are smaller than that of the PM structure.

These results show that the phonon scattering and anharmonicity in FM/AFM monolayer MnPS$_3$ are enhanced significantly. Moreover, the Grüneisen parameter varies inversely with the bond strength of the material.[42,43] Therefore, the FM/AFM phases have weaker bonding interaction compared with the PM phase, which is in agreement with our aforementioned simulation results.

4 Conclusions

In conclusion, we systematically investigated the structural deformation, lattice vibration and thermal conductivity of monolayer MnPS$_3$ with PM/FM/AFM phases. The structural parameters of monolayer MnPS$_3$ with different magnetic ordering were analyzed, and the order of bonding strength is PM > FM > AFM phase. Remarkable impact of magnetic ordering on phonon spectrum were also observed. The thermal conductivity of the FM/AFM phases is lower than the PM one. The magnetic ordering-dependent phonon properties were further analyzed to explain the obtained results. Our study provides an insight into magnetic ordering-dependent phonon behavior and suggests a possibility for MnPS$_3$-based thermal switching devices.

Conflicts of interest

The authors have no conflicts to disclose.

Acknowledgements

References

1 C. Gong, L. Li, Z. Li, H. Ji, A. Stern, Y. Xia, T. Cao, W. Bao, C. Wang and Y. Wang, *Nature*, 2017, **546**, 265–269.
2 J. Cenker, B. Huang, N. Suri, P. Thijssen, A. Miller, T. Song, T. Taniguchi, K. Watanabe, M. A. McGuire and D. Xiao, *Nat. Phys.*, 2021, **17**, 20–25.
3 C. Gong and X. Zhang, *Science*, 2019, **363**, eaav4450.
4 S. Wolf, D. Awschalom, R. Buhrman, J. Daughton, S. von Molnár, M. Roukes, A. Y. Chtchelkanova and D. Treger, *Science*, 2001, **294**, 1488–1495.
5 J. Ma, X. Xi, Y. Li and X. Sun, *Nat. Nanotechnol.*, 2021, **16**, 576–583.
6 H. Li, P. Zhang, T. Ouyang, H. Wang, J. Li, C. He, C. Zhang and C. Tang, *Appl. Phys. Lett.*, 2022, **120**, 092403.
7 G. Qin, H. Wang, L. Zhang, Z. Qin and M. Hu, *J. Mater. Chem. C*, 2020, **8**, 3520–3526.
8 K. Wang, X. Xu, Y. Cheng, M. Zhang, J.-S. Wang, H. Wang and G. Zhang, *Appl. Phys. Lett.*, 2021, **118**, 023102.
9 Y. Liu, Q. Liu, Y. Liu, X. Jiang, X. Zhang and J. Zhao, *Nanoscale*, 2021, **13**, 7714–7722.
10 K. Wang, W. Zhou, Y. Cheng, M. Zhang, H. Wang and G. Zhang, *Nanoscale*, 2021, **13**, 10882–10890.
11 V. Baltz, A. Manchon, M. Tsoi, T. Moriyama, T. Ono and Y. Tserkovnyak, *Rev. Mod. Phys.*, 2018, **90**, 015005.
12 D. Torelli, H. Moustafa, K. W. Jacobsen and T. Olsen, *npj Comput. Mater.*, 2020, **6**, 1–12.
13 L. Jin, L. Wang, X. Zhang, Y. Liu, X. Dai, H. Gao and G. Liu, *Nanoscale*, 2021, **13**, 5901–5909.
14 Y. M. Bunkov, E. Alakshin, R. Gazizulin, A. Klochkov, V. Kuzmin, V. L'vov and M. Tagirov, *Phys. Rev. Lett.*, 2012, **108**, 177002.
15 I. M. Alliati, R. F. Evans, K. S. Novoselov and E. J. Santos, *npj Comput. Mater.*, 2022, **8**, 1–9.
16 V. Ivády, T. Simon, J. R. Maze, I. Abrikosov and A. Gali, *Phys. Rev. B: Condens. Matter Mater. Phys.*, 2014, **90**, 235205.
17 G. Long, H. Henck, M. Gibertini, D. Dumcenco, Z. Wang, T. Taniguchi, K. Watanabe, E. Giannini and A. F. Morpurgo, *Nano Lett.*, 2020, **20**, 2452–2459.
18 M. Birowska, P. E. F. Junior, J. Fabian and J. Kunstmann, *Phys. Rev. B*, 2021, **103**, L121108.
19 R.-C. Xiao, D.-F. Shao, Y.-H. Li and H. Jiang, *npj Quantum Mater.*, 2021, **6**, 1–6.
20 J. Yang, Y. Zhou, Q. Guo, Y. Dedkov and E. Voloshina, *RSC Adv.*, 2020, **10**, 851–864.
21 J. Hafner, *J. Comput. Chem.*, 2008, **29**, 2044–2078.
22 M. Ernzerhof and G. E. Scuseria, *J. Chem. Phys.*, 1999, **110**, 5029–5036.
23 A. Rohrbach, J. Hafner and G. Kresse, *J. Phys.: Condens. Matter*, 2003, **15**, 979.
24 D. Zhang, Y. Hu, H. Zhong, S. Yuan and C. Liu, *Nanoscale*, 2019, **11**, 13800–13806.
25 D. Zhang, S. Hu, Y. Sun, X. Liu, H. Wang, H. Wang, Y. Chen and Y. Ni, *ES Energy Environ.*, 2020, **10**, 59–65.
26 Y. Ouyang, C. Yu, J. He, P. Jiang, W. Ren and J. Chen, *Phys. Rev. B*, 2022, **105**, 115202.
27 F. Eriksson, E. Fransson and P. Erhart, *Adv. Theory Simul.*, 2019, **2**, 1800184.
28 W. Li, J. Carrete, N. A. Katcho and N. Mingo, *Comput. Phys. Commun.*, 2014, **185**, 1747–1758.
29 M. Jiang, K. Xu, N. Liao and H. Zhou, *Appl. Surf. Sci.*, 2021, **543**, 148846.
30 Y. Zhang, W. Wang, M. Huang, P. Liu, G. Hu, C. Feng, X. Lei, M. Gu, H. Yang and K. Liu, *Nanoscale*, 2020, **12**, 23266–23273.
31 B. L. Chittari, Y. Park, D. Lee, M. Han, A. H. MacDonald, E. Hwang and J. Jung, *Phys. Rev. B*, 2016, **94**, 184428.
32 I. Cabria and A. A. El-Meligi, *Int. J. Hydrogen Energy*, 2018, **43**, 5903–5912.
33 D. H. Luong, T. L. Phan, G. Ghimire, D. L. Duong and Y. H. Lee, *APL Mater.*, 2019, **7**, 081102.
34 M. Gibertini, M. Koperski, A. F. Morpurgo and K. S. Novoselov, *Nat. Nanotechnol.*, 2019, **14**, 408–419.
35 Y. Yin, Y. Hu, S. Li, G. Ding, S. Wang, D. Li and G. Zhang, *Nano Res.*, 2022, **15**, 3818–3824.
36 J. Chen, J. He, D. Pan, X. Wang, N. Yang, J. Zhu, S. A. Yang and G. Zhang, *Sci. China: Phys., Mech. Astron.*, 2022, **65**, 117002.
37 X. Yang, T. Feng, J. Li and X. Ruan, *Phys. Rev. B*, 2019, **100**, 245203.
38 Y. Xia, *Appl. Phys. Lett.*, 2018, **113**, 073901.
39 J. Yu, T. Li, G. Nie, B.-P. Zhang and Q. Sun, *Nanoscale*, 2019, **11**, 10306–10313.
40 Y. Ni, D. Zhang, X. Liu, H. Wang, Y. Chen, Y. Xia and H. Wang, *J. Chem. Phys.*, 2021, **155**, 204701.
41 B. Peng, H. Zhang, H. Shao, Y. Xu, G. Ni, R. Zhang and H. Zhu, *Phys. Rev. B*, 2016, **94**, 245420.
42 X. Su, N. Zhao, S. Hao, C. C. Stoumpos, M. Liu, H. Chen, H. Xie, Q. Zhang, C. Wolverton and X. Tang, *Adv. Funct. Mater.*, 2019, **29**, 1806534.
43 Z.-F. Cheng and R.-L. Zheng, *Chin. Phys. Lett.*, 2016, **33**, 046501.